Optical Coherence Tomography-Based Patient-Specific Coronary Artery Reconstruction and Fluid-Structure Interaction Simulation

Jiaqiu Wang

School of Chemistry, Physics and Mechanical Engineering, Queensland University of Technology, Brisbane 4000, Australia

jiaqiu.wang@hdr.qut.edu.au

Phani Kumari Paritala

School of Chemistry, Physics and Mechanical Engineering, Queensland University of Technology, Brisbane 4000, Australia

phanikumari.paritala@hdr.qut.edu.au

Jessica Benitez Mendieta

School of Chemistry, Physics and Mechanical Engineering, Queensland University of Technology, Brisbane 4000, Australia

jessica.benitezmendieta@hdr.qut.edu.au

Yo Komori

Deformation Control Lab, Hokkaido University, Hokkaido 060-8628, Japan

k8m9r0@gmail.com

Owen Christopher Raffel

Department of Cardiology, The Prince Charles Hospital, Brisbane 4032 Australia

School of Medicine, University of Queensland, St Lucia, Brisbane 4072, Australia

christopher.raffel@health.qld.gov.au

Yuantong Gu

School of Chemistry, Physics and Mechanical Engineering, Queensland University of Technology, Brisbane 4000, Australia

yuantong.gu@qut.edu.au

Zhiyong Li *(Corresponding)*

School of Chemistry, Physics and Mechanical Engineering, Queensland University of Technology, Brisbane 4000, Australia

School of Biological Science & Medical Engineering, Southeast University, Nanjing 210096, China

zylicam@gmail.com

Abstract

Plaque rupture is related to the mechanical stress it suffered. The value and distribution of the mechanical stress in plaque could help on assessing plaque vulnerability. To look into the stress conditions in the coronary artery, a patient-specific coronary model was created by using optical coherence tomography (OCT) and angiography imaging data. The reconstructed coronary model consisted of the structure of the lumen, the arterial wall and plaque components. Benefited by the high resolution of OCT, detailed structures such as the thin fibrous cap could be observed and built into the geometry. On this reconstructed coronary model, a fully-coupled fluid-structure interaction (FSI) simulation was performed. The principle stress in coronary plaque and the wall shear stress (WSS) were analysed.

The FSI simulation results show that the cap thickness had significant effect on the stress, and the principle stress at the thin cap area was more than double of those at the locations with a larger thickness. WSS is thought as an important parameter to assess the potentially dangerous areas of the atherosclerosis-prone (caused by low WSS) and the plaque rupture (high WSS). From the WSS plots of our FSI model, the area with abnormal WSS value was detected around the position where a lipid core existed. The FSI simulation results were compared with the results from the conventional structure-only and the computational fluid dynamics (CFD)-only computational models to quantify the difference between the three models. We found little difference in the principle stress results between the FSI and the structure-only model, but a significant difference between the FSI and the CFD-only model when looking into the WSS. The WSS values at the two observation spots from the CFD-only model were higher than the values from the FSI model by 17.95% and 22.66% in average, respectively. Furthermore, the FSI model detected more areas of low WSS, because the fluid domain could expand circumferentially when pressure loaded on the flexible arterial.

This study suggests that OCT-based FSI model may be useful for plaque vulnerability assessment and it may be critical to perform the FSI simulation if an accurate WSS value is required.

Keywords: Plaque Rupture; Optical Coherence Tomography; Coronary Reconstruction; Fluid-structure Interaction

I. Introduction

Cardiovascular diseases, especially the coronary heart diseases are the leading causes of morbidity and mortality globally (Benjamin *et al.*, 2018)(Townsend *et al.*, 2016)(Australian Institute of Health and Welfare, 2018). Among the causes of acute coronary syndromes such as plaque rupture, erosion, and calcific nodule, plaque rupture is responsible for more than half of acute coronary syndromes (Mehta *et al.*, 2016). This kind of rupture-prone plaque is named as vulnerable plaque, commonly they have some morphological characterizations, such as thin-cap fibroatheroma, lipid-rich necrotic core and et al. (Naghavi *et al.*, 2003)(Insull, 2009). For diagnosis purpose, medical imaging modalities are used to detect the coronary morphology. Non-invasive methods, such as computed tomography (CT) and magnetic resonance imaging (MRI), are widely used in coronary angiography. Invasive catheter-based imaging method, intravascular ultrasound (IVUS) and optical coherence tomography (OCT), could identify different plaque components, such as calcification, fibrous cap and lipid-rich core (Vancraeynest *et al.*, 2011)(Escolar *et al.*, 2006)(Prati *et al.*, 2010). IVUS has been established as the golden standard for *in vivo* coronary imaging (Garcìa-Garcìa *et al.*, 2011). OCT provides a higher spatial resolution (10-15 μm) than IVUS, and it may be better in quantifying the thickness of the fibrous cap (Regar *et al.*, 2003). However, besides the invasiveness, the main limitation of OCT is the low image penetration of 1 to 2.5 mm (Lowe *et al.*, 2011).

The 3D model of coronary arteries could be reconstructed based on the medical imaging technologies. The coronary model can be reconstructed by using angiography (Garreau *et al.*, 1991)(Guggenheim *et al.*, 1991)(Messenger *et al.*, 2000)(Auricchio *et al.*, 2014), and the model reconstructed from angiography only contains the lumen part (i.e. the fluid domain) of coronary. The frequently used method for coronary plaque reconstruction is by combining the IVUS and angiography imaging data. This method stacks IVUS slices on a 3D curve path, which is generated from the biplane digital subtraction angiograms (DSA). Besides the lumen geometry, this model could also show the structure of the arterial wall including different type of tissue and plaque (Laban *et al.*, 2004)(Bourantas *et al.*, 2005)(Doulaverakis *et al.*, 2013). In a similar way, coronary model can be reconstructed by using OCT data. Coronary lumen models reconstructed based on OCT have been used on in-silico study of stenosis (Kousera *et al.*, 2014) and stent implementation (Ellwein *et al.*, 2011). Recently, OCT data has been used to segment the coronary plaque cap thickness in a model combining with angiography and IVUS (Guo *et al.*, 2017). However, based on our knowledge, there has not been a report which uses OCT and angiography to reconstruct the 3D patient-specific coronary model that includes both the structure of the lumen and the arterial wall.

Based on the reconstructed model, computational simulation can provide biomechanical factors to look into the mechanism of plaque rupture. From a mechanical point of view, blood vessel suffers tensile stress and wall shear stress (WSS). Blood pressure is loaded perpendicularly to the vessel wall, and consequently the cylindrical structure of vessel wall is stretched, which produced a circumferential stress. A high value of tensile stress may cause the rupture of the fibrous cap. WSS acts longitudinally on the arterial wall surface and it is induced by the difference between the movement of blood flow and the vessel wall (Kwak *et al.*, 2014). A low value of WSS is relevant to atherosclerosis-prone area, while a high value of WSS is one of the causative factors promoting the development of high-risk plaques (Dolan, Kolega and Meng, 2013)(Eshtehardi *et al.*, 2017). Finite element method (FEM) could simulate the blood vessel's deformation and calculate the tensile stress inside the blood vessel (Li *et al.*, 2006)(Li *et al.*, 2007)(Gao *et al.*, 2009b). While to calculate the WSS, computational fluid dynamics (CFD) is often based on finite volume method (FVM) to perform simulation (Long *et al.*, 2000)(Augst *et al.*, 2003)(Dong, Wong and Tu, 2013). A fluid-structure interaction (FSI) simulation couples the FEM and FVM methods, from which both tensile stress and WSS could

be calculated (Tang *et al.*, 2005)(Gao *et al.*, 2009a)(Gholipour *et al.*, 2018). Not like the homogenous load in structural-only analysis and the rigid wall in CFD-only model, FSI provides the data transfer of force and displacement on the fluid-structure interaction surface (Chimakurthi *et al.*, 2018).

In this paper, a 3D patient-specific coronary model was created by combining intravascular-OCT and angiography imaging data. This model included the structure of lumen, arterial wall and plaque lipid core. On this coronary model, a fully-coupled FSI simulation was performed to look into the distribution of the tensile stress and the WSS in coronary artery during one cardiac cycle. To discuss the advantage of our OCT-based FSI model, these results were also compared with the results from the structural-only and the CFD-only computational models using the same geometric model.

II. Data Acquisition, Models, and Methods

A. Data Acquisition

The coronary OCT and the angiography imaging data were acquired from the Catheterization Laboratory in The Prince Charles Hospital (Chermside, QLD, Australia). In this study, a set of right coronary artery (RCA) imaging data from a 61-year-old male patient with acute coronary syndrome (ACS) was used. This study was approved by the internal review board and informed written consent was obtained.

B. 3D Coronary Reconstruction

The geometry for an FSI simulation contains both structure and fluid domain. From OCT the contours of the lumen and the plaque were obtained. As the intravascular-OCT is a catheter-based imaging modality, each contour has to be stacked and aligned with the catheter path-line to form a 3D coronary model. This required 3D baseline could be generated from the angiography data, which was used as the guidance during the OCT operation.

Two plane angiographic images from two different directions were selected to generate the 3D baseline of the coronary artery. The central line of the coronary artery in each angiography imaging was segmented in ImageJ (imagej.nih.gov/ij/), the segmented central line was outputted as a set of 2D discrete point coordinates (Figure 1(c)). These coordinates from the two plane angiography data were imported into SolidWorks (Dassault Systèmes, Vélizy-Villacoublay, France). In SolidWorks, these two splines in 2D planes were projected to form a new spline in 3D space. Finally, the 3D spline was discretised into a set of registration points and their 3D coordinates were exported. The number of these discrete points was determined by the corresponding OCT slice number.

The OCT images were recorded in the axial direction during the pull back of catheter in the coronary artery. Each slice provided a 2D view of the coronary lumen and vessel wall in the radial direction. In each slice, contours of the lumen, the outer wall boundary, and plaque component were segmented by using ImageJ (Figure 1(a)&(b)).

An in-house developed Matlab (R2017a, MathWorks, Natick, MA, US) code package was used to register the 2D OCT contours onto the 3D angiographic baseline. The Matlab code was designed to have several functional packages, which contains all the sub-steps in the registration processes. Because of the difference in the resolution of the OCT and the angiography, the program firstly unified the scale of the point coordinates from the OCT and the angiography into the millimetre unit. Then in each OCT slice, the centroid was defined as the midpoint on the perpendicular bisector of the longest line segment between the two points on the lumen contour. Then each contour in each 2D OCT slice was moved to their position in 3D space by offsetting the centroid point onto the corresponding registration point on the 3D

angiography baseline. Considering the tortuous of coronary arteries, each OCT slice should be vertical against the local baseline curvature. A slope angle of each slice (from the normal vector of OCT slice plane to the local tangent vector of 3D baseline) was determined by calculating and applying a rotational matrix to each OCT slice (Figure 1(d)).

The transferred point coordinates were imported into the ANSYS SpaceClaim, a Geometry component in ANSYS Workbench (version 19.0, ANSYS, Canonsburg, PA, USA). Here the contours from each slice, including the coronary lumen, the outer boundary, and plaque component, were re-generated in a 3D space using the point coordinates (Figure 1(e)). Then based on the contours, the surface of the coronary lumen, the outer wall and the plaque were created separately by blending each kind of contours. Finally, the geometric model of the coronary lumen, the outer wall and the plaque were generated by solidifying their surfaces and performing Boolean operation on the overlapped parts between the outer wall, the lumen and the plaque (Figure 1(f)).

To save the computational consumption, the coronary model was cut off so that only the part of coronary model we were interested in (the part with a plaque) was kept for the subsequent fluid-structure simulation, the length of the region of interest was approximately 3 times of the length of the plaque.

C. Structural Computational Model

In the structural part, the mesh size function was chosen as proximity and curvature. To avoid large distortion, a small growth rate of 1.10 was given. The coronary artery and the plaque were assumed as isotropic and linear elastic with different material parameters (Paritala *et al.*, 2018). The material parameters were listed in Table 1. The two small surfaces at the coronary vessel wall ends were given fixed support (Figure 1(f)). The inner surface of the arterial wall was set as fluid solid interface for data transfer in FSI. No other load was applied to the structural participant, and the blood vessel only received the pressure transferred from the fluid participant. The bonded contact was given at the contact region between the normal tissue and the lipid core, and pure penalty formulation was chosen for the contact pair computation.

D. Fluid Computational Model

In order to perform the FSI, dynamic mesh was enabled for the fluid domain, and the diffusion and remesh functions were given as dynamic mesh setting. Adaptive mesh size function with coarse size of 0.30 mm was selected for the fluid mesh. Also, a 5-layer inflation was added to the lateral surface of the fluid. The mesh size guaranteed there was no negative cell volume error when performing simulation with a big relative timestep selected (>= 0.005 s).

The boundary wall was defined as system coupling. Blood flow through the coronary artery was assumed as laminar incompressible, homogeneous and Newtonian. The viscosity was set to 0.00345 Pa·s, and the density was set to 1050 kg/m^3 (Liu and Tang, 2011). Velocity boundary condition was prescribed at the inlet and pressure boundary condition was given to the outlet. Based on the number of timesteps in the CFD simulation, the velocity and pressure waveforms were interpolated to a set of discrete points. As the geometry we used for the FSI simulation was only a short section of the whole vessel, the flow was not fully developed from the inlet. To obtain a fully developed parabolic flow profiles as the boundary condition for the subsequent FSI simulation, a CFD-only model with expended inlet and outlet was performed. Later the velocity profiles defined by the node coordinates and the velocity components were directly given to the inlet of the fluid part in the FSI simulation (Figure 2).

E. Computational Simulation Setting

The FSI simulation was performed on ANSYS Workbench platform. System coupling component was used for the pressure/force and displacement data transfer between the two participants in FSI, i.e. transient structural and CFD. No-slip conditions and normal stress equilibrium conditions were assumed at all interfaces. The calculation time step was set to 0.01s, running for two cardiac cycles. To help on stability of the coupled simulation, at each time step, the transferring data values were ramped linearly in the first 5 coupling iterations (minimum iteration number). To avoid the instability of the results from initial time steps, only the result data from the second cycle was used for post-processing.

To compare with our FSI model, the conventional structural-only and CFD-only simulations were conducted based on the same geometry in the FSI simulation. In the transient structural analysis in ANSYS Workbench, the fluid-structure interface on the inner surface of arterial wall was replaced by direct pressure load, while other settings were kept same as in the FSI simulation. The pressure was loaded as a time-dependent table with the time step 0.01 s, whose value at each time-step came from the pressure profile applied on the fluid outlet in the previous FSI setup. In the CFD-only simulation, the same setting was given as FSI model but disabling dynamic mesh and removing the system coupling interface.

III. Results

A. Principle Stress

From the structural analysis part, we analysed the stress distribution in the plaque area. We created two planes crossing the lipid core where the principle stresses P1 were plotted. The thin fibrous cap is one of the morphological features of a rupture-prone plaque, and we found the maximum value of the principle stress always occurred at the spot connecting to the lipid area where the cap thickness was also relatively thin. It is because the lipid part was relatively more flexible than the arterial fibrous tissue, the deformation at these spots always had a large deformation determined by their surrounding structure and force load. In this FSI model, the driving force of the arterial wall deformation came from the pressure transferred from the fluid domain, therefore we could observe that the tendency of stress – P1 was correlated with the pressure curve (Figure 3).

On an enlarged arterial wall plane view (t = 0.5s, where the pressure load was in the middle range out of one cycle), we selected two spots on the arterial wall tissue connecting to the lipid core. One spot located on the thin cap area, where the cap thickness was 0.081 mm, and the value of stress - P1 at this point was 120.3 kPa. Another point with a relative thick wall (thickness = 0.264 mm), where the stress – P1 was only 57.7 kPa. Comparing these two selected points, the thickness of the thin cap was less than 1/3 of the thick cap in other areas, and the value of the principle stress was more than double of those at the locations with a larger thickness. Furthermore, we plotted the principle stresses of these two points throughout one cardia cycle (one-second-period with sampling rate of 0.05s). The variation stress - P1 followed the tendency of pressure load. The stress- P1 value at the thin cap area was always double or more than double of the value at the thick cap area (Figure 4).

By comparing the principle stress results from the FSI and the structure-only model, we found there was not a significate difference between these two models. For example, the values of stress-P1 in one cardiac cycle at a selected point from these two models were plotted in Figure 5. Both the curves of stress-P1 trended following the pressure wave, and there was no significant difference on the stress-P1 results between the two models.

B. Wall Shear Stress

From CFD participant, WSS was used to reveal atherosclerosis-prone area (with low WSS value) and rupture-prone area (with high WSS value). WSS has a positive correlation to the fluid velocity. In the coronary artery, it is more likely to observe a high WSS value at stenosis part and at the time point with a high velocity flow, and vice versa. To look into the low WSS, we selected the fluid domain data at time step of 0.1s, when the fluid velocity was low. To emphasize the low WSS area, a local scale from 0 to 2 Pa was used. The WSS contours were plotted in Figure 6(a), the minimum WSS in this area was 0.344 Pa. On the contrary, at the time step of 0.6 s with a high fluid velocity, the WSS contours were plotted to detect the high WSS area (Figure 6(b), in local scale WSS > 6 Pa). The maximum WSS value at this area reached to 14.14 Pa. It is noticed that the WSS value at the area close to the lipid core (named as Position-1) was lower than the area opposite the lipid core (named as Position-2). It was because (a) the deformation of the arterial wall near the lipid part was larger than the opposite part, which made the geometry of the fluid domain expand inconsistently in the circumferential direction; (b) the flow velocity profile at this fluid area was not the ideal-parabolic shape as it was at inlet, because the flow has developed through an irregular vessel tube. Thus the irregular velocity profile caused the unbalance circumferential distribution of WSS.

Further, we plotted the WSS at these two selected positions in one cardiac cycle with a sampling rate of 0.05s. The value of WSS varied following the flow velocity changing. Also we labelled the area where WSS < 2 Pa or WSS > 6 Pa. We can see at Position-1, in one cardiac cycle, there was half of the period where the WSS was more than 6 Pa. And at Position-2, the period when WSS was less than 2 Pa took up more than 2/3 of one cardiac cycle. This meant at these two positions, the blood vessel suffered the 'vulnerable' WSS over half of the time during each cardiac cycle, the potentially dangerous areas of the atherosclerosis-prone (caused by low WSS) and the plaque rupture (high WSS).

At the two selected positions 1 and 2 in Figure 6, the values of WSS from both FSI and CFD-only models were plotted together (Figure 7). In the plot, the waves of WSS varied following the tendency of the fluid velocity. At each position, the WSS value from the CFD-only model was always higher than that from the FSI model. From statistics, at Position-1 the WSS value from the CFD-only was higher than the value from the FSI by 17.95% in average (ranged from 3.39% to 45.90%). At Position-2, the difference of WSS value between these two models was 22.66 % (from 7.84% to 36.63%).

In Figure 8, the WSS contours at time step of 0.8 s were plotted, by comparing these results from the FSI and the CFD-only model, the area where WSS < 2 Pa in the FSI model was larger than that in CFD-only model. Further, we plotted the curves of the low WSS area where its value was < 2 Pa in the selected segment (Figure 8(c)), including the results from the FSI model, the FSI model without plaque (same geometry of arterial wall but without a lipid core) and the CFD-only model. The area of low WSS was negatively correlated to the flow velocity wave. The FSI model detected more area of the low WSS, because the fluid domain could expand circumferentially when pressure loaded on the flexible arterial. Since the lipid core was removed, the FSI model without a lipid core was not flexible as the original FSI model, therefore less low WSS area was found. The CFD-only model showed least area of WSS < 2 Pa because of the non-deformable rigid wall.

Besides comparing the WSS value at each time step. The time-averaged wall shear stress (TaWSS) throughout one cardiac cycle is also a key derived parameter related to plaque vulnerability assessment. The TaWSS of the FSI model and the CFD-only model were plotted in Figure 9(a)&(b). The values of the TaWSS from the CFD-only model ware higher than those of the FSI model at the same locations. For example, at the same point in the plaque area, the

value of TaWSS were 6.369 Pa and 8.222 Pa in the FSI model and the CFD-only model, respectively. Figure 9(c)&(d) shows the histograms of TaWSS value range distribution from the FSI model and the CFD-only models. From the statistics, the TaWSS in the FSI model concentrated on the low (0~3 Pa) and medium (3~6 Pa) value range, while the distribution of TaWSS in the CFD-only model was more dispersive. There were more areas with a high TaWSS value in the CFD-only model than in the FSI model.

IV. Discussion

A. Advantage of OCT-based Geometric Model

FSI is a viable method that can be used to simulate the in-tube flow with flexible boundary wall, just like a blood vessel. Therefore the FSI is now popularly used in various in-silico studies in cardiovascular research. However, due to the limitation of methods of imaging and reconstruction, the patient-specific coronary model is not always available. Instead, tube-like idealized model (Tang *et al.*, 2004)(Gholipour *et al.*, 2018) were used. Such an idealized model emphasized the characterization of the blood vessel, such as the stenosis part and plaque component, and also it could generate separated layers of the vessel. Another advantage of using the idealized model is the parameters of the blood vessel can be adjusted, which makes it easy to change the geometric shape and study the influence from different structures by controlling variables. However, an idealized model missed a lot of geometric information because of the uniqueness of patient coronary.

Alternatively, since the CT- and MRI-angiography are commonly used in coronary imaging and from them it is easy to reconstruct patient-specific coronary lumen model. Uniform thickness arterial wall could be extruded based on the patient-specific lumen model (Dong *et al.*, 2015). Such kind of model provides flexible arterial wall and gives better results compared with the lumen-only CFD model. The disadvantage of this kind of model is lacking of the plaque geometry inside the arterial wall, so only the homogenous material properties could be given to the arterial wall.

Compared with the idealized and simplified model, the patient-specific model provides the real structure of coronary lumen, arterial wall and plaque component, including IVUS- and OCT-based models. They have a similar imaging and reconstruction process. Compared with OCT-based model, IVUS has the virtual histology (VH) which could help in the automatic segmentation (Wang *et al.*, 2015). Also the coronary outer wall is easier to be segmented in IVUS slices than in OCT. However, the superiority of OCT is that the high resolution of the image provides the accurate cap thickness (Guo *et al.*, 2017). Therefore the OCT-based model may provide a more accurate plaque structural information thus has the advantage to be used for future biomechanical analysis, which can help with the assessment of plaque vulnerability.

B. Advantage of FSI Computational Model

From the results of the principle stress from the FSI model and the structural-only model, we found there was no significant difference on the stress-P1 results between the two models. In the structural-only model, the uniform pressure was loaded to the inner arterial wall, while in the FSI model, the force was given node by node from the CFD result. However, there was a small variation on each node's force value, because the pressure, as the dominate force component, did not change sharply in the CFD simulation within a relevant short flow length. Therefore there was little difference on the deformation of geometry between these two models, hence the stress results were similar. However, if the flow domain is long, or with a complex structure (for example, bifurcation or branch), the pressure distribution may be more inhomogeneous distributed, so the difference between the stress analysis based on the FSI model and the structural-only model may be more significant. In the coronary model, we can

conclude that a structure-only model could be an approximation to the FSI model, if the structural stress result is required only. It can provide an approximate result and with a much less computation consumption. A similar finding was also reported by previous studies (Huang *et al.*, 2016).

In the comparison between the FSI model and the CFD-only model, we have noticed that there were significant differences in WSS values between the FSI and the CFD-only model. To understand why the WSS values in the FSI model were lower than those in the CFD-only model, we plotted three lumen contours at a selected plane from the CFD-only model and the FSI model at the time points with the min and the max pressure values (Figure 10). The lumen expanded after pressure was applied, and a higher pressure led to a larger lumen. As the inlet boundary conditions (velocity profile) were the same between the CFD-only model and the FSI model, the larger lumen in the FSI model would certainly result in a decrease in local velocities. As the WSS has a positive correlation with the velocity value, we could see the WSS was lower in the FSI model compared with the CFD-only model. Besides the deformation of the lumen contours, the centroids of the lumen contours were also shifted, it was because the coronary was forced to bend in the cardiac cycle in the FSI modelling. Therefore, putting together, the results of the WSS would be significantly different compared with the CFD-only model with a rigid boundary. For future analysis of blood flow in coronary artery, it may be critical to perform FSI simulation if an accurate WSS value is required.

C. Limitations

OCT provides an ultra-high resolution of the arterial structure, but due to the limitation of low penetration (1 to 2 mm), it is hard to distinguish the deep structure of the arterial wall. This has been a big challenge when segmenting the outer wall boundary. In this study, the outer wall boundary contours were estimated with the help from the interventional cardiologists based on their extensive experience in OCT imaging. Therefore, the contours of the outer wall in this model might not be as accurate as the contours of the lumen and the lipid core which appeared clear boundaries in the OCT imaging. To investigate the impact of the estimation on the modelling results, we performed a sensitivity analysis of the outer boundary estimation. The analysis suggests that the outer wall boundary estimation based on OCT imaging could provide reasonable results in WSS calculation if the error of the estimated outer boundary could be controlled within a small range. The details of the sensitivity analysis can be found in the complementary material. Furthermore, limited by the imaging resolution, it is still a challenge to reconstruct the three layers, e.g. intima, media and adventitia of arterial vessel in the patient-specific coronary model.

The other main limitation of this study is that we have not included the pre-shrinkage procedure. There are a few previous studies (Huang *et al.*, 2009)(Zhu *et al.*, 2010)(Guo *et al.*, 2017) where a uniform circumferential shrink and axial stretch ratio was used. However, we have performed a study using an idealized tube model to estimate the shrink ratio and found the shrink ratio of the lumen contour and the outer wall boundary were no the same (please refer to complementary material). Based on the current data, we were not able to determine the unloaded geometry or the zero-stress state. Furthermore, we performed an analysis to discuss a possible strategy which may be used to determine the pre-shrink ratio in future studies. Further details can be found in the complimentary material.

Moreover, in our FSI simulation, the deformation was caused by the pulsatile flow only. In reality, the coronary artery also has cyclic bending caused by the myocardial cyclic movement. Lastly, the geometry, the mechanical properties and the fluid conditions may vary between different individuals, so it is not possible to reach clinical useful conclusion based on this single patient study and it will be helpful to plan a large-scale clinical study based the

developed methodology in the future. In this study the WSS range we used were low WSS < 2 Pa and high WSS > 6 Pa. From literatures, other thresholds were used as low WSS of 1 Pa and high WSS of 2.5 Pa, 3 Pa and 7 Pa (Eshtehardi *et al.*, 2017)(Dolan, Kolega and Meng, 2013)(Malek, 1999). The blood vessels from different patients may have unequable 'vulnerable' WSS range, and it is impossible to know the exact threshold of patient-specific value of low and high WSS. A common standard of the low, high and normal WSS threshold could be proposed through massive patient data analysis in the future.

V. Conclusion

In this study, we used OCT imaging combined with CT-angiography to reconstruct patient-specific coronary model. The ultra-high resolution of OCT provided a clear view of the coronary arterial structure and plaque components, especially the thin fibrous cap. The reconstructed model was used for the FSI simulation, which coupled the structural analysis and CFD analysis. The result from the FSI simulation provided the information about the tensile stress and the WSS. By comparing the FSI computational model with the structural-only and the CFD-only computational models, little difference was found in the principle stress values between the FSI model and the structure-only model, but there was a significant difference between the FSI model and the CFD-only model when looking into the result of WSS. FSI can provide not only the stress distribution within the plaque, but also the realistic fluid flow analysis within the coronary artery. Therefore, it may be critical to perform the FSI simulation if an accurate WSS value is required.

VI. Acknowledgement

Computational resources and services used in this work were provided by the HPC and Research Support Group, Queensland University of Technology, Brisbane, Australia.

VII. Funding

This work was supported in part by the National Natural Science Foundation of China (NSFC) (Grant no. 11772093, 61821002), Australian Research Council (ARC) (FT140101152, DP180103009), and the Prince Charles Hospital Foundation (NI2019-19).

VIII. Compliance with ethical standards

Conflict of interest

The authors declare that they have no conflict of interest.

Ethics

The QUT University Human Research Ethics Committee assessed this research as meeting the conditions for exemption from HREC review and approval in accordance with section 5.1.22 of the National Statement on Ethical Conduct in Human Research (2007).

IX. Reference

Augst, A. D. *et al.* (2003) 'Accuracy and Reproducibility of CFD Predicted Wall Shear Stress Using 3D Ultrasound Images', *Journal of Biomechanical Engineering*, 125(2), p. 218. doi: 10.1115/1.1553973.

Auricchio, F. *et al.* (2014) 'A simple framework to generate 3D patient-specific model of coronary artery bifurcation from single-plane angiographic images', *Computers in Biology*

and Medicine. Elsevier, 44(1), pp. 97–109. doi: 10.1016/j.compbiomed.2013.10.027.

Australian Institute of Health and Welfare (2018) *Australia ' s health 2018: in brief*. doi: 10.1145/3173574.3174019.

Benjamin, E. J. *et al.* (2018) *Heart disease and stroke statistics - 2018 update: A report from the American Heart Association*, *Circulation*. doi: 10.1161/CIR.0000000000000558.

Bourantas, C. V. *et al.* (2005) 'A method for 3D reconstruction of coronary arteries using biplane angiography and intravascular ultrasound images', *Computerized Medical Imaging and Graphics*, 29(8), pp. 597–606. doi: 10.1016/j.compmedimag.2005.07.001.

Chimakurthi, S. K. *et al.* (2018) 'ANSYS Workbench System Coupling: a state-of-the-art computational framework for analyzing multiphysics problems', *Engineering with Computers*. Springer London, 34(2), pp. 385–411. doi: 10.1007/s00366-017-0548-4.

Dolan, J. M., Kolega, J. and Meng, H. (2013) 'High wall shear stress and spatial gradients in vascular pathology: A review', *Annals of Biomedical Engineering*, 41(7), pp. 1411–1427. doi: 10.1007/s10439-012-0695-0.

Dong, J. *et al.* (2015) 'Fluid–structure interaction analysis of the left coronary artery with variable angulation', *Computer Methods in Biomechanics and Biomedical Engineering*. Taylor & Francis, pp. 1500–1508. doi: 10.1080/10255842.2014.921682.

Dong, J., Wong, K. K. L. and Tu, J. (2013) 'Hemodynamics analysis of patient-specific carotid bifurcation: A CFD model of downstream peripheral vascular impedance', *International Journal for Numerical Methods in Biomedical Engineering*, 29(4), pp. 476–491. doi: 10.1002/cnm.2529.

Doulaverakis, C. *et al.* (2013) 'IVUSAngio Tool: A publicly available software for fast and accurate 3D reconstruction of coronary arteries', *Computers in Biology and Medicine*. Elsevier, 43(11), pp. 1793–1803. doi: 10.1016/j.compbiomed.2013.08.013.

Ellwein, L. M. *et al.* (2011) 'Optical Coherence Tomography for Patient-specific 3D Artery Reconstruction and Evaluation of Wall Shear Stress in a Left Circumflex Coronary Artery', *Cardiovascular Engineering and Technology*, 2(3), pp. 212–227. doi: 10.1007/s13239-011-0047-5.

Escolar, E. *et al.* (2006) 'New imaging techniques for diagnosing coronary artery disease.', *CMAJ : Canadian Medical Association journal = journal de l'Association medicale canadienne*, 174(4), pp. 487–95. doi: 10.1503/cmaj.050925.

Eshtehardi, P. *et al.* (2017) 'High wall shear stress and high-risk plaque: an emerging concept', *International Journal of Cardiovascular Imaging*. Springer Netherlands, 33(7), pp. 1089–1099. doi: 10.1007/s10554-016-1055-1.

Gao, H. *et al.* (2009a) 'Carotid arterial plaque stress analysis using fluid-structure interactive simulation based on in-vivo magnetic resonance images of four patients', *Journal of Biomechanics*, 42(10), pp. 1416–1423. doi: 10.1016/j.jbiomech.2009.04.010.

Gao, H. *et al.* (2009b) 'Study of reproducibility of human arterial plaque reconstruction and its effects on stress analysis based on multispectral in vivo magnetic resonance imaging', *Journal of Magnetic Resonance Imaging*, 30(1), pp. 85–93. doi: 10.1002/jmri.21799.

Garcìa-Garcìa, H. M. *et al.* (2011) 'IVUS-based imaging modalities for tissue characterization: Similarities and differences', *International Journal of Cardiovascular Imaging*, 27(2), pp. 215–224. doi: 10.1007/s10554-010-9789-7.

Garreau, M. *et al.* (1991) 'A knowledge-based approach for 3-D reconstruction and labeling of vascular networks from biplane angiographic projections.', *IEEE transactions on*

medical imaging, 10(2), pp. 122–31. doi: 10.1109/42.79469.

Gholipour, A. *et al.* (2018) 'Three-dimensional biomechanics of coronary arteries', *International Journal of Engineering Science*. Elsevier Ltd, 130, pp. 93–114. doi: 10.1016/j.ijengsci.2018.03.002.

Guggenheim, N. *et al.* (1991) 'Spatial reconstruction of coronary arteries from angiographic images', *Physics in Medicine and Biology*, 36(1), pp. 99–110. doi: 10.1088/0031-9155/36/1/009.

Guo, X. *et al.* (2017) 'Combining IVUS and Optical Coherence Tomography for More Accurate Coronary Cap Thickness Quantification and Stress/Strain Calculations: A Patient-Specific Three-Dimensional Fluid-Structure Interaction Modeling Approach', *Journal of Biomechanical Engineering*, 140(April), pp. 1–12. doi: 10.1115/1.4038263.

Huang, X. *et al.* (2009) 'Patient-Specific Artery Shrinkage and 3D Zero-Stress State in Multi-Component 3D FSI Models for Carotid Atherosclerotic Plaques Based on In Vivo MRI Data NIH Public Access', *Mol Cell Biomech*, 6(2), pp. 121–134. Available at: https://www.ncbi.nlm.nih.gov/pmc/articles/PMC2681261/pdf/nihms89307.pdf.

Huang, X. *et al.* (2016) '3D MRI-based multicomponent thin layer structure only plaque models for atherosclerotic plaques', *Journal of Biomechanics*. Elsevier, 49(13), pp. 2726–2733. doi: 10.1016/j.jbiomech.2016.06.002.

Insull, W. (2009) 'The Pathology of Atherosclerosis: Plaque Development and Plaque Responses to Medical Treatment', *American Journal of Medicine*. Elsevier Inc. Elsevier Inc., 122(1 SUPPL.), pp. S3–S14. doi: 10.1016/j.amjmed.2008.10.013.

Kousera, C. A. *et al.* (2014) 'Patient-specific coronary stenoses can be modeled using a combination of OCT and flow velocities to accurately predict hyperemic pressure gradients', *IEEE Transactions on Biomedical Engineering*, 61(6), pp. 1902–1913. doi: 10.1109/TBME.2014.2310954.

Kwak, B. R. *et al.* (2014) 'Biomechanical factors in atherosclerosis: Mechanisms and clinical implications', *European Heart Journal*, 35(43), pp. 3013–3020. doi: 10.1093/eurheartj/ehu353.

Laban, M. *et al.* (2004) 'ANGUS: a new approach to three-dimensional reconstruction of coronary vessels by combined use of angiography and intravascular ultrasound', in *Computers in Cardiology 1995*. IEEE, pp. 325–328. doi: 10.1109/CIC.1995.482638.

Li, Z. Y. *et al.* (2006) 'Stress analysis of carotid plaque rupture based on in vivo high resolution MRI', *Journal of Biomechanics*, 39(14), pp. 2611–2622. doi: 10.1016/j.jbiomech.2005.08.022.

Li, Z. Y. *et al.* (2007) 'Structural analysis and magnetic resonance imaging predict plaque vulnerability: A study comparing symptomatic and asymptomatic individuals', *Journal of Vascular Surgery*, 45(4), pp. 768–775. doi: 10.1016/j.jvs.2006.12.065.

Liu, B. and Tang, D. (2011) 'Influence of non-Newtonian properties of blood on the wall shear stress in human atherosclerotic right coronary arteries.', *Molecular & cellular biomechanics : MCB*, 8(1), pp. 73–90. doi: 10.3970/mcb.2011.008.073.

Long, Q. *et al.* (2000) 'Reconstruction of blood flow patterns in a human carotid bifurcation: A combined CFD and MRI study', *Journal of Magnetic Resonance Imaging*, 11(3), pp. 299–311. doi: 10.1002/(SICI)1522-2586(200003)11:3<299::AID-JMRI9>3.0.CO;2-M.

Lowe, H. C. *et al.* (2011) 'Intracoronary optical diagnostics: Current status, limitations, and potential', *JACC: Cardiovascular Interventions*. Elsevier Inc., 4(12), pp. 1257–1270. doi: 10.1016/j.jcin.2011.08.015.

Malek, A. M. (1999) 'Hemodynamic Shear Stress and Its Role in Atherosclerosis', *JAMA*, 282(21), p. 2035. doi: 10.1001/jama.282.21.2035.

Mehta, L. S. *et al.* (2016) *Acute Myocardial Infarction in Women : A Scientific Statement from the American Heart Association*, *Circulation*. doi: 10.1161/CIR.0000000000000351.

Messenger, J. C. *et al.* (2000) '3D coronary reconstruction from routine single-plane coronary angiograms: Clinical validation and quantitative analysis of the right coronary artery in 100 patients', *International Journal of Cardiac Imaging*, 16(6), pp. 413–427. doi: 10.1023/A:1010643426720.

Naghavi, M. *et al.* (2003) 'From vulnerable plaque to vulnerable patient: a call for new definitions and risk assessment strategies: Part I.', *Circulation*, 108(15), pp. 1772–8. doi: 10.1161/01.CIR.0000087481.55887.C9.

Paritala, P. K. *et al.* (2018) 'Numerical investigation of atherosclerotic plaque rupture using optical coherence tomography imaging and XFEM', *Engineering Fracture Mechanics*. Elsevier, 204(November), pp. 531–541. doi: 10.1016/j.engfracmech.2018.11.002.

Prati, F. *et al.* (2010) 'Expert review document on methodology, terminology, and clinical applications of optical coherence tomography: physical principles, methodology of image acquisition, and clinical application for assessment of coronary arteries and atherosclerosis.', *European heart journal*, 31(4), pp. 401–15. doi: 10.1093/eurheartj/ehp433.

Regar, E. *et al.* (2003) 'Optical coherence tomography', *Cardiovascular Radiation Medicine*, 4(4), pp. 198–204. doi: 10.1016/j.carrad.2003.12.003.

Tang, D. *et al.* (2004) 'Effect of a Lipid Pool on Stress/Strain Distributions in Stenotic Arteries: 3-D Fluid-Structure Interactions (FSI) Models', *Journal of Biomechanical Engineering*, 126(3), p. 363. doi: 10.1115/1.1762898.

Tang, D. *et al.* (2005) 'Quantifying Effects of Plaque Structure and Material Properties on Stress Distributions in Human Atherosclerotic Plaques Using 3D FSI Models', *Journal of Biomechanical Engineering*, 127(7), p. 1185. doi: 10.1115/1.2073668.

Townsend, N. *et al.* (2016) 'Cardiovascular disease in Europe: epidemiological update 2016', *European Heart Journal*, 37(42), pp. 3232–3245. doi: 10.1093/eurheartj/ehw334.

Vancraeynest, D. *et al.* (2011) 'Imaging the vulnerable plaque', *Journal of the American College of Cardiology*, 57(20), pp. 1961–1979. doi: 10.1016/j.jacc.2011.02.018.

Wang, L. *et al.* (2015) 'Morphological and Stress Vulnerability Indices for Human Coronary Plaques and Their Correlations with Cap Thickness and Lipid Percent: An IVUS-Based Fluid-Structure Interaction Multi-patient Study', *PLoS Computational Biology*, 11(12), pp. 1–15. doi: 10.1371/journal.pcbi.1004652.

Zhu, C. *et al.* (2010) 'Normalized Wall Index Specific and MRI-Based Stress Analysis of Atherosclerotic Carotid Plaques', *Circulation Journal*, 74(11), pp. 2360–2364. doi: 10.1253/circj.CJ-10-0305.

Table 1 Material properties used for the arterial and plaque lipid tissue.

	Young's Modulus	Poisson's Ratio
Arterial Tissue	0.6 MPa	0.48
Lipid Core	0.02 MPa	0.48

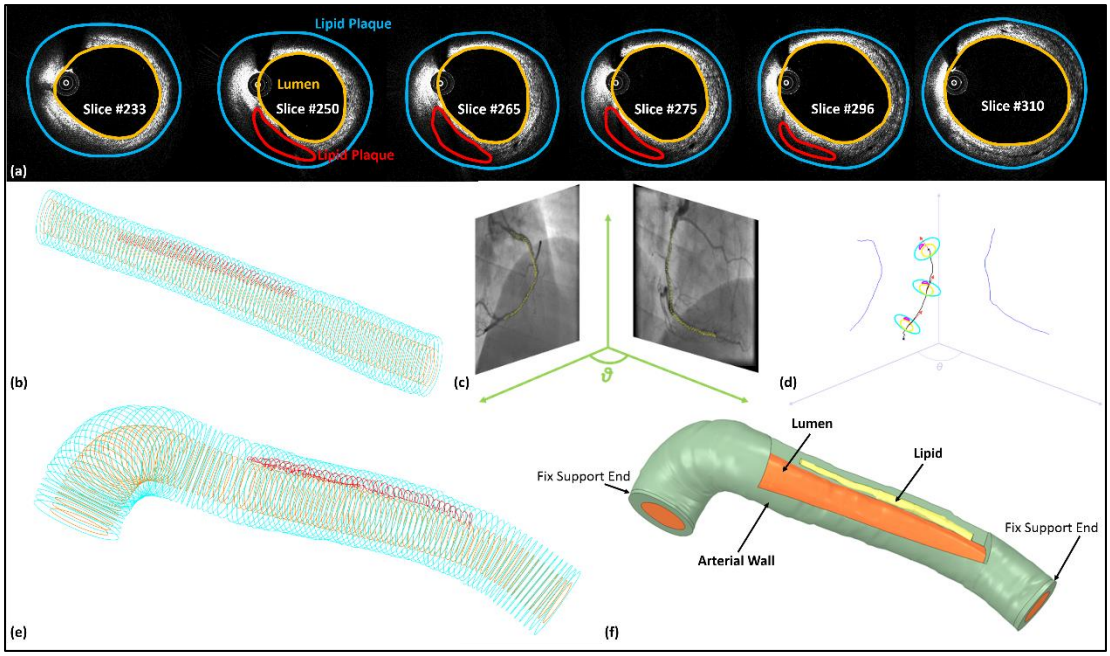

Figure 1 Patient-specific coronary model reconstruction. (a) Contours of lumen, outer wall, and component (lipid core) were segmented on several example OCT slices. (b) The sequence of the segmented OCT contours. (c) The bi-plane angiographic imaging used to reconstruct the 3D coronary baseline. (d) The diagram of 3D coronary baseline and the registration process of OCT contours. (e) The contours from OCT were registered on 3D baseline. (f) The geometry of patient-specific coronary, including the structure of arterial wall, lumen and lipid core. Note there are two small surface at vessel wall ends for fix supports.

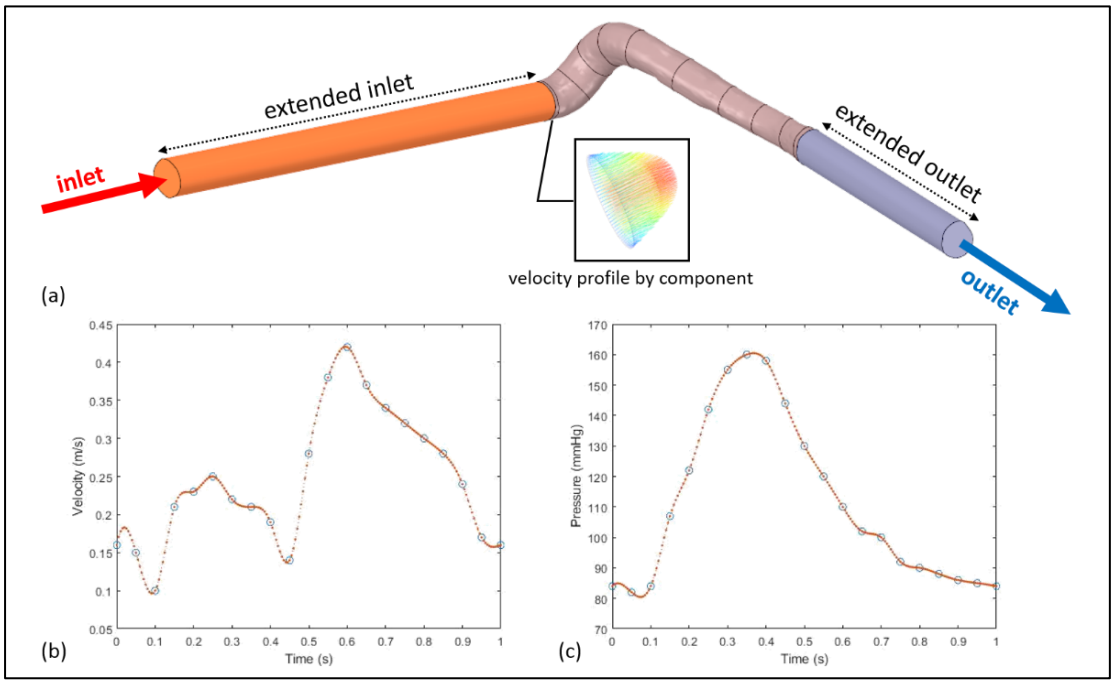

Figure 2 The boundary conditions given to the fluid domain. (a) The coronary lumen model with extended inlet and outlet, the emphasized box shows the fully-developed flow profile defined by the velocity component that was given to the inlet in the FSI simulation. (b) & (c) the time-dependent profiles of velocity given to the inlet and of pressure given to the outlet.

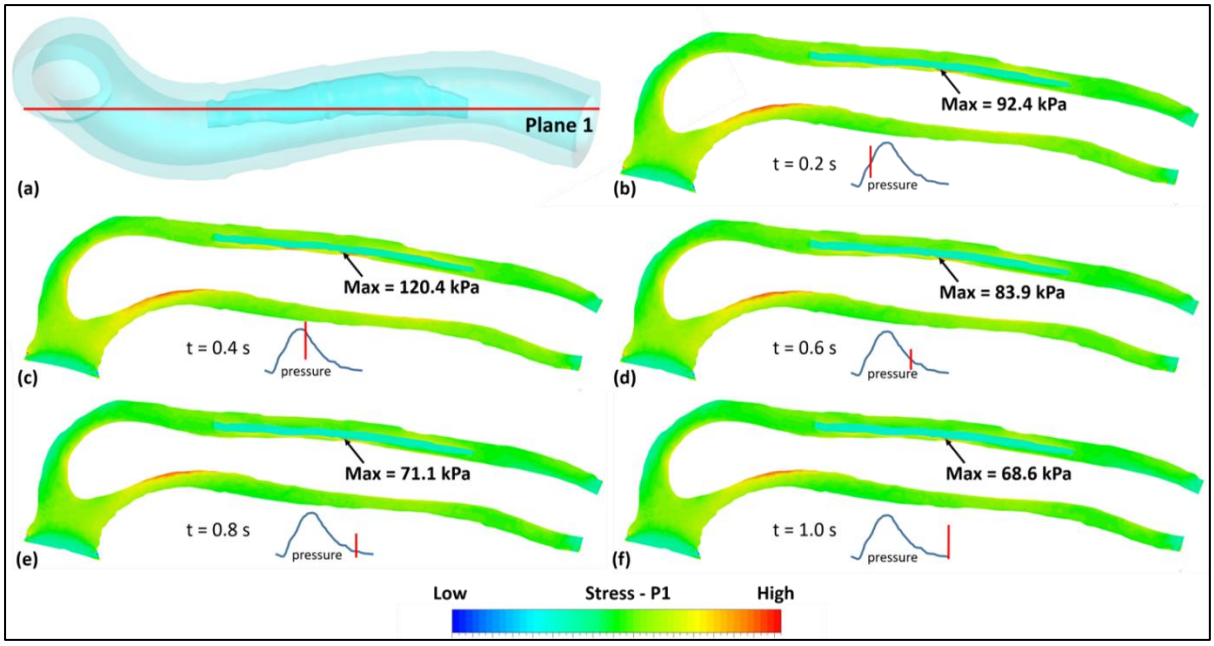

Figure 3 A plane view of the principle stress (stress – P1) inside the coronary arterial wall. (a) the position of plane, the plane was cut across the lipid core. (b)~(f) the maximum value of the principle stress at the thin cap area inside the coronary vessel at each time step.

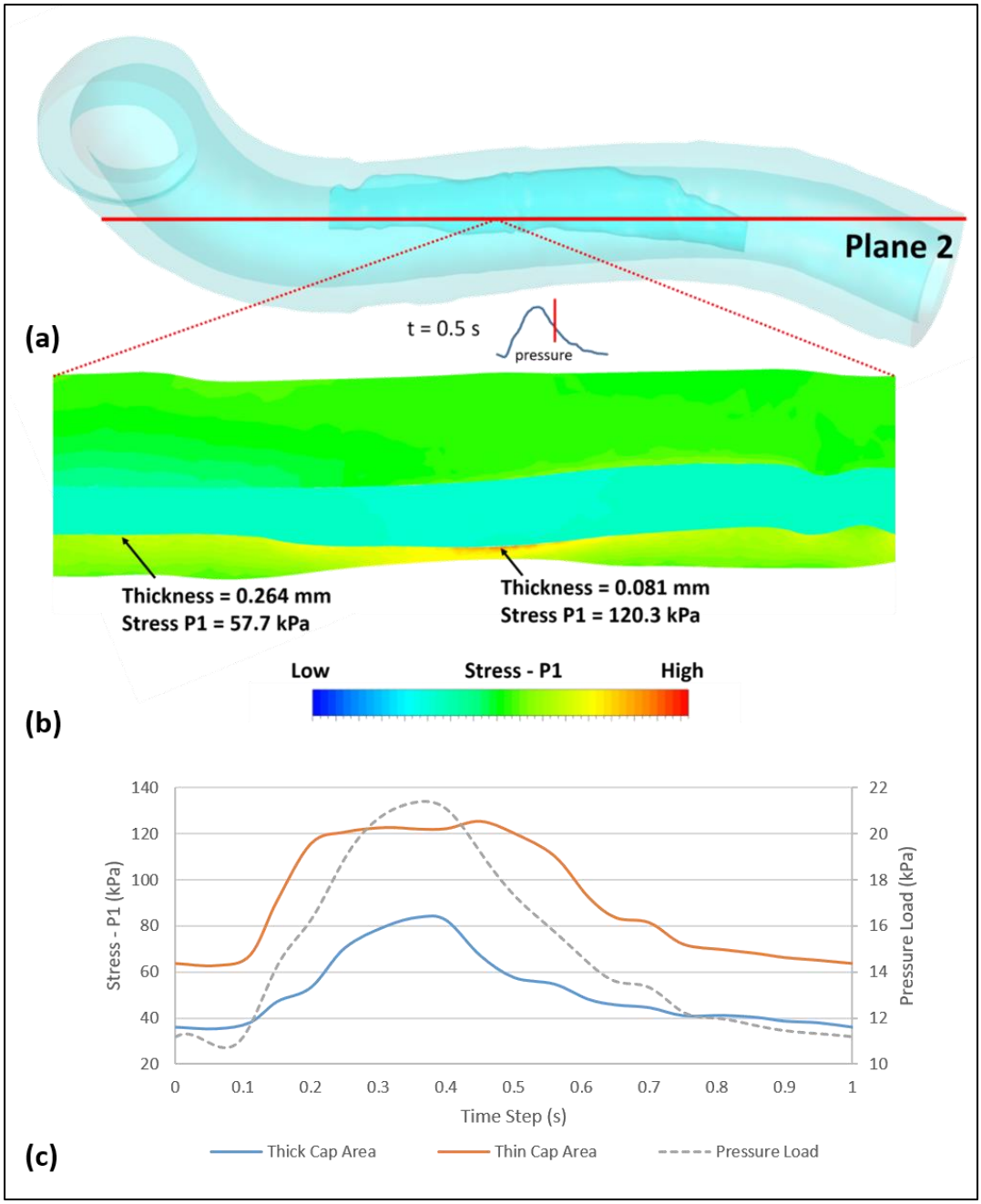

Figure 4 Comparison of the principle stresses between the thin and the thick cap area. (a) A local view of the principle stress (stress – P1) on Plane 2 inside the coronary arterial wall at the time of 0.5 s. (b) The thickness of the thin cap area (0.081 mm) was less than 1/3 of the thick area (0.264 mm). High principle stress value was observed at the thin cap area, where the value (120.3 kPa) was more than 2 times of the value at the point with a larger thickness (57.5 kPa). (c)The plot of the principle stresses at these two selected points throughout a cardiac cycle (sampling rate = 0.05 s). The variation stress - P1 followed the tendency of pressure load. The stress- P1 value at the thin cap area was always double or more of the value at the thick cap area.

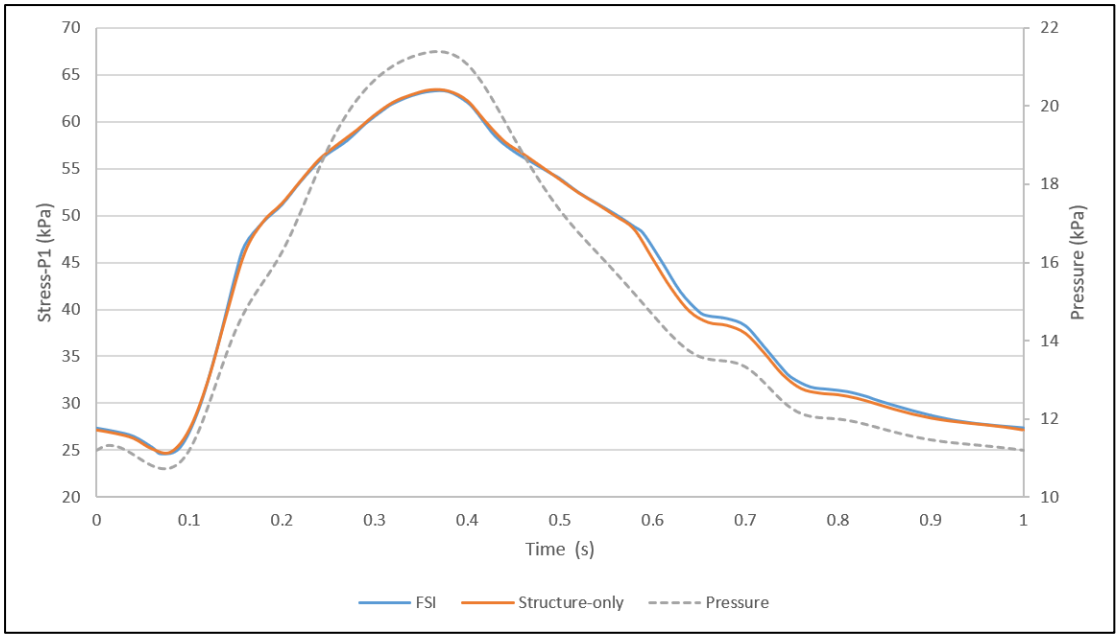

Figure 5 The comparison of the principle stress at a selected point between the FSI model and the structure-only model. The value of stress-P1 followed the pressure wave. There was not a significant difference in the results between the FSI model and the structure-only model.

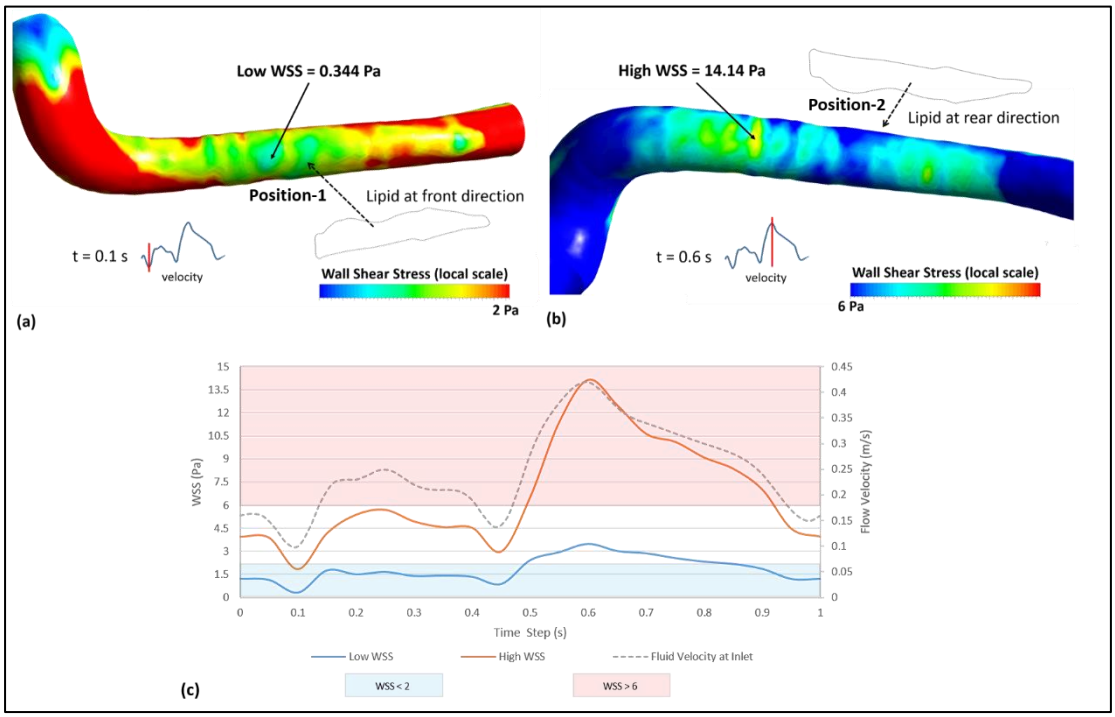

Figure 6 Low and high WSS contour examples. (a) At time 0.1s, the fluid velocity was low. Low WSS area (in green and yellow colour) was found at the area near the lipid core (Position-1), the minimum WSS at this area was 0.344 Pa. Local scale was used, all area where WSS > 2 Pa was in red. (b) At time 0.6s, the fluid velocity was high. High WSS area (in light yellow and green colour) was found in the area opposite the lipid core (Position-2), the maximum WSS in this area was 14.14 Pa. Local scale was used, all area where WSS < 6 Pa was in blue. (c) The curves of WSS at these two points (the point with low WSS in blue while with high WSS in red) throughout one cardiac cycle (1 s with sampling rate of 0.05 s). The value of WSS varied following the flow velocity changing (dash curve in grey). The area where WSS < 2 Pa or WSS > 6 Pa were labelled in light blue and red boxes respectively.

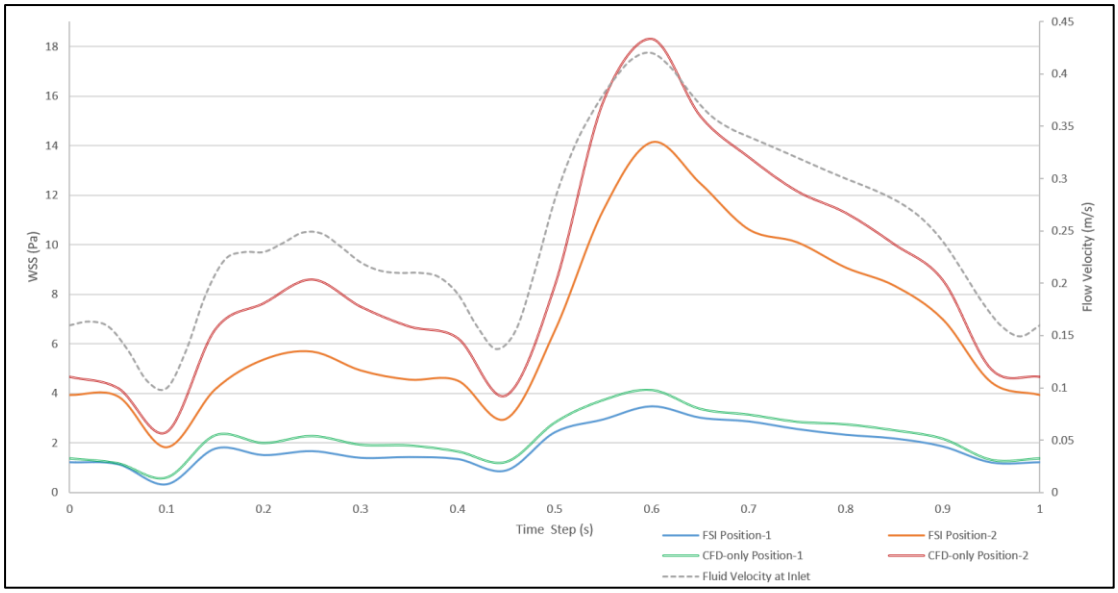

Figure 7 The WSS value at selected Position-1 and 2 from the FSI model and the CFD-only model in one cardiac cycle. The waves of WSS varied following the tendency of fluid velocity. At each position, the WSS value from the CFD-only model was always higher than the value from the FSI model.

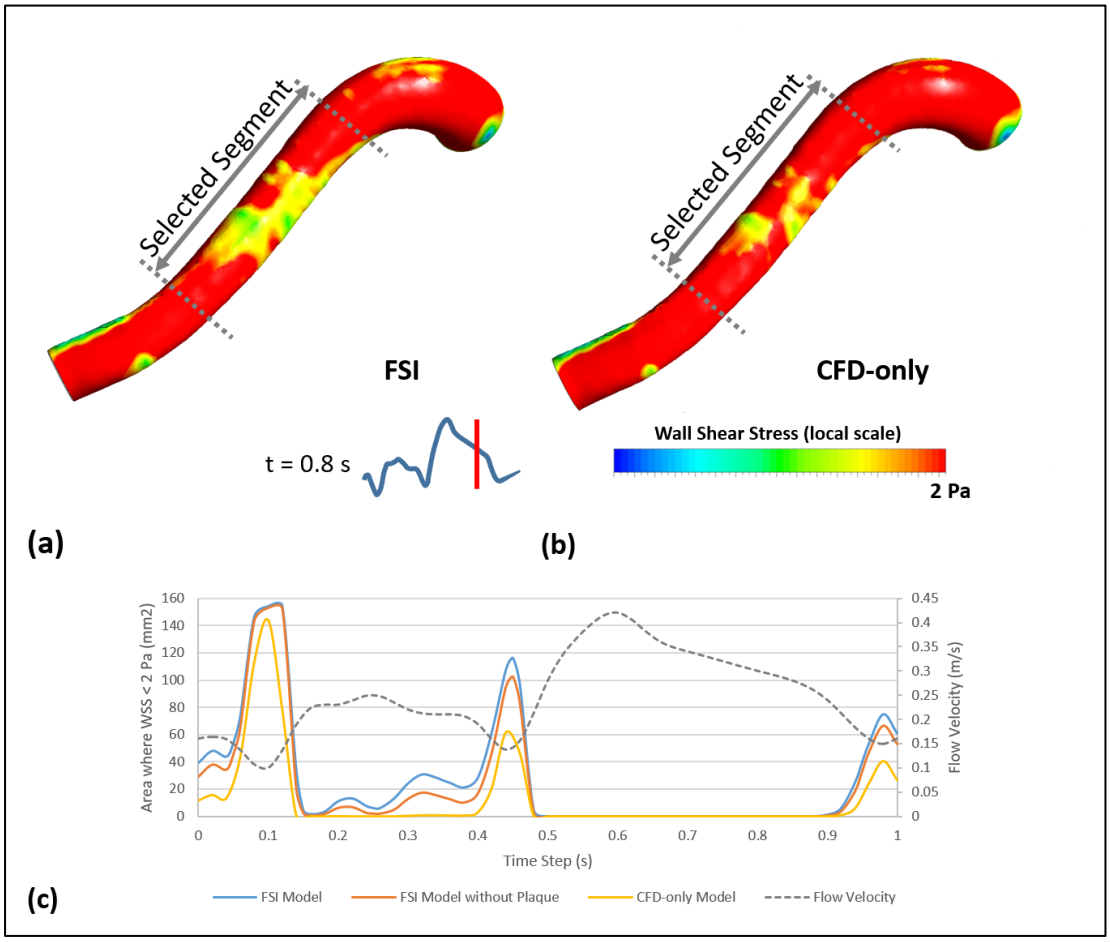

Figure 8 Comparison between the FSI model and the CFD-only model. (a)&(b) The results of low WSS < 2 Pa (in local scale) at time step of 0.8 s. The low WSS area in the FSI model was larger than in the CFD-only model. (c) Within a selected segment of the coronary model, the area where WSS < 2 Pa were plotted through one cardiac

cycle. The area of low WSS is negative correlated with the flow velocity wave, and the FSI model always detected more areas of low WSS than the CFD-only model.

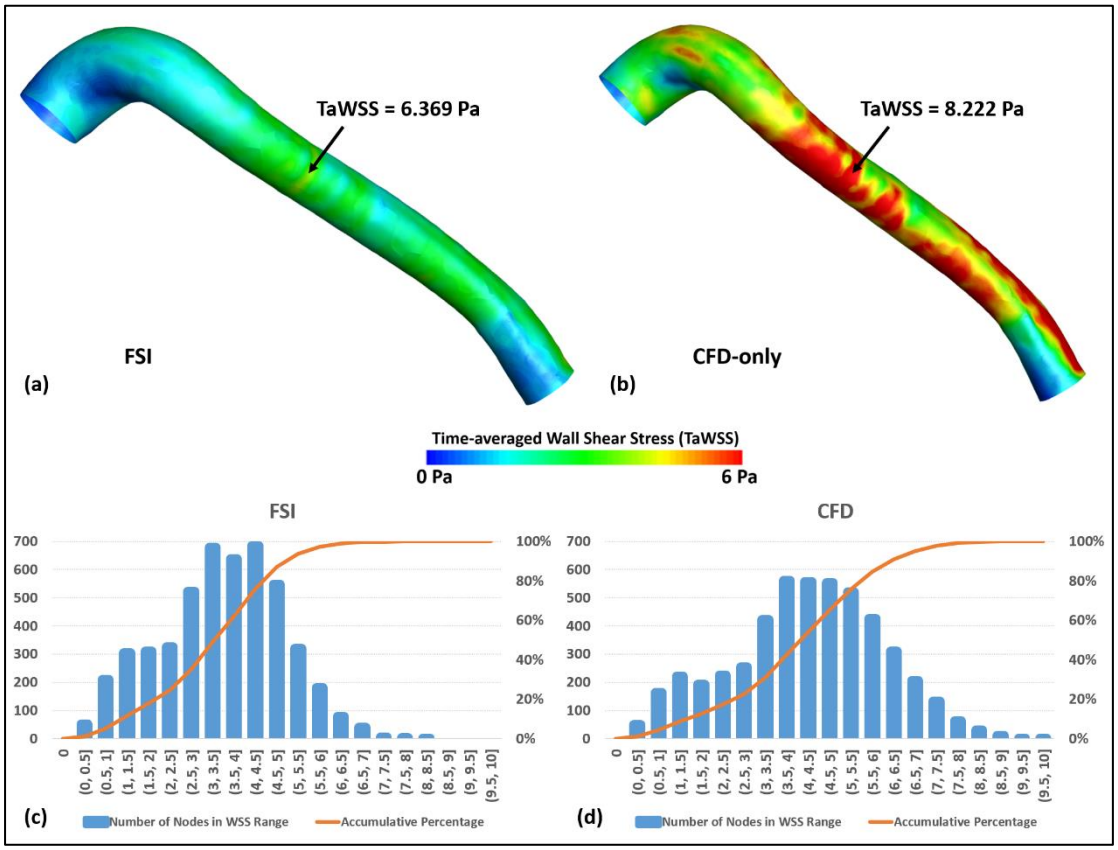

Figure 9 Time-averaged wall shear stress (TaWSS). (a)&(b) TaWSS plot of the FSI model and the CFD-only model. Generally at the same location, the value of TaWSS of the FSI model was lower than that of the CFD-only model. At the same point in the plaque area, the value of TaWSS were 6.369 Pa and 8.222 Pa in the FSI and CFD-only model, respectively. (c)&(d) The histogram of TaWSS value range distribution. The TaWSS of the FSI model concentrated on the low and medium value range, while the distribution of TaWSS of the CFD-model was more dispersive.

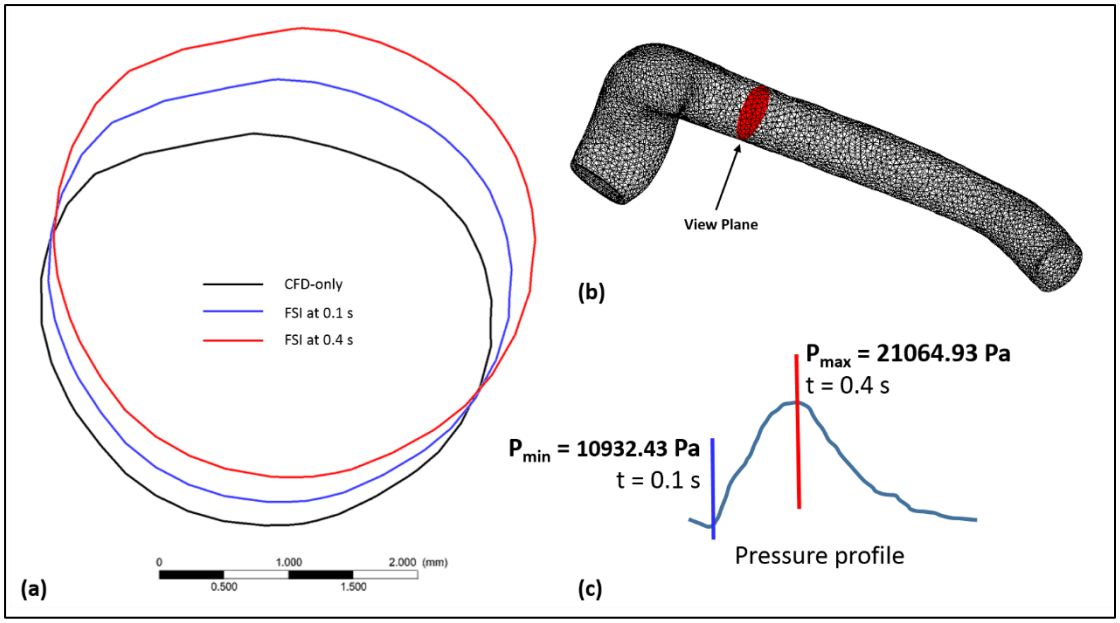

Figure 10 An example of lumen contour variation at a plane view during a cardiac cycle. (a) The contours from the CFD-only model and the FSI model at 0.1s and 0.4s time points. (b) The plane location in the model. (c) The lumen deformation was correlated with the pressure profile. The two time points with the maximum and the minimum pressure values were selected.